CONFIDENTIAL REVIEW COPY. DO NOT DISTRIBUTE.

Using Nasal Curves Matching for Expression Robust 3D Nose Recognition

Anonymous BTAS 2013 submission

Abstract

The development of 3D face recognition algorithms that are robust to variations in expression has been a challenge for researchers over the past decade. One approach to this problem is to utilize the most stable parts on the face surface. The nasal region's relatively constant structure over various expressions makes it attractive for robust recognition. In this paper, a new recognition algorithm is introduced that is based on features from the three dimensional shape of nose. After denoising, face cropping and alignment, the nose region is cropped and 16 landmarks robustly detected on its surface. Pairs of landmarks are connected, which results in 75 curves on the nasal surface; these curves form the feature set. The most stable curves over different expressions and occlusions due to glasses are selected using forward sequential feature selection (FSFS). Finally, the selected curves are used for recognition. The Bosphorus dataset is used for feature selection and FRGC v2.0 for recognition. The results show highest recognition ranks than any previously obtained using the nose region: 1) 82.58% rank-one recognition rate using only two training samples with varying expression, for 505 different subjects and 4879 samples; 2) 90.01% and 80.01% when Spring2003 is used for training and Fall2003 and Spring2004 for testing in the FRGC v2.0 dataset, for neutral and varying expressions, respectively.

1. Introduction

The nasal region is relatively a stable part on the face and compared to the other parts such as the forehead, eyes, cheeks, and mouth, its structure is comparatively consistent over different expressions [1, 4, 3]. It is also one of the parts of the face that is least prone to occlusions caused by hair and scarves [5]. Indeed, it is very difficult to deliberately occlude the nose region without attracting suspicion [7]. In addition, the unique convex structure of the nasal region makes its detection and segmentation more straightforward than other parts of the face, particularly in 3D.

The nasal region therefore has a number of advantageous properties for use as a biometric. However, it has been suggested that the texture and color information of the 2D nose region does not provide enough discrimination for human authentication [16]. This problem as been ameliorated by the developments in high resolution 3D facial imaging over the last decade, which have led a number of researchers to start studying the potential of the nose region for human authentication and identification. One of the main motivations for this is to overcome the problems posed by variations in expression which can significantly influence the performance of face recognition algorithms.

A good example of the use of the nasal region to recognize people over different expressions is the approach of Chang *et al*. [1]. Here, face detection is performed using color segmentation and then thresholding of the curvature is used to segment different regions around the nose region. The iterative closest point (ICP) and principal component analysis (PCA) algorithms are applied for recognition. Using the FRGC v2.0 dataset to evaluate the algorithm's performance, a significant drop in recognition performance was found for varying expressions (from 91% to 61.5% and from 77.7% to 61.3% for ICP and PCA, respectively). In an alternative approach, the 2D and 3D information of the nose region are used for pattern rejection, to reduce the size of face gallery [6]. A more recent use of the nose region for 3D face recognition is that of Drira *et al*. [4]. Geodesic contours, centralized on the nose tip, are localized on the nose region using the Dijkstra algorithm and the distances between the sets of contours for each nose are used for recognition. Performance was evaluated on a smaller subset of FRGC containing 125 different subjects and the rank-one recognition was 77%. It should also be noted that this algorithm is not capable of processing faces with open mouths.

Another nose region-based face recognition algorithm is introduced in [3]. The nose is first segmented using curvature information and the pose is corrected before applying the ICP algorithm for recognition. Using the Bosphorus dataset (105 subjects, with average 30 samples per subject), the rank-one recognition was reported as 79.41% for samples with pose variation and 94.10% for frontal view faces. Moorhouse *et al*. applied holistic and landmark-based approaches for 3D nose recognition [7]. A small subset of 23 subjects from the Photoface dataset [15], which is based on

the photometric stereo, was used for evaluation. A variety of features were used for recognition but despite the small sample, the highest rank-one recognition achieved was only 47%.

This paper proposes a new recognition technique using the nasal region. Using robustly defined landmarks around the edge of the nose, a collection of curves connecting the landmarks are defined on the nose surface and these form the feature vectors. The approach is termed the Nasal Curve Matching (NCM) algorithm. The algorithm starts by preprocessing the input data. Images are denoised, the face is cropped and then aligned using Mian *et al.*'s iterative PCA algorithm [6]. Then, the nose region is cropped and a landmarking algorithm used to detect 16 fiducial points around the nose region. Taking the landmarks in pairs, the intersection of orthogonal planes passing through each pair with the face region defines the facial curves. The resulting curves are normalized and used as the feature vectors. Finally, feature selection is used to extract the features that are most robust to variations in expression.

The NCM algorithm employs a simple, yet effective algorithm for nose region landmarking and then derives a set of curves that are used for 3D recognition using the nose region. The proposed algorithm's accuracy is verified using the recognition ranks over the FRGC v2.0 dataset [8], which is higher than the previous approaches using the nasal region. For example, FRGC's experiment 3 resulted in 90.1% and 80.01% rank-one recognition for neutral and varying expressions, respectively. Results for the Bosphorus dataset [9] are also presented.

The remainder of this paper is organized as follows. First, in section 2, the preprocessing algorithm is explained. Section 3 describes the landmarking algorithm and the construction of the nasal curves, and the feature selection is explained in section 4. The experimental results, including the feature selection and classification performance are presented in Section 5. Finally, conclusions are drawn in section 6.

2. Preprocessing

Preprocessing is a vital step in the face recognition systems. Its performance can significantly affect the recognition performance and rest of the algorithm, for example by degrading the feature extraction and the feature's correspondence between samples. As a consequence, the within-class similarity and between-class dissimilarity might be lost. Here, a 3 stage preprocessing approach is employed. First, the data is denoised and the face region is cropped. Then, the face is aligned and resampled using a PCA-based pose correction algorithm and finally the nose region is cropped.

2.1. Denoising, tip detection and face cropping

3D face images are usually degraded by impulsive noise, holes and missing data. Although the noise effects are more salient on the depth $\mathbf{Z}$ information, the $\mathbf{X}$ and $\mathbf{Y}$ coordinates can also be affected. In order to remove the noise in $\mathbf{X}$ the standard deviation of each column is first calculated. Columns with high standard deviations will contain noise while the columns with low standard deviations are relatively noise free. Therefore, the two neighboring columns with the lowest standard deviation are found and the $\mathbf{X}$ map's slope is computed. The slope is then used to resample the map. The same procedure is performed to denoise the $\mathbf{Y}$ map. The only difference is that the standard deviation is computed for the map's rows. The $\mathbf{Z}$ map is resampled using the new $\mathbf{X}$ and $\mathbf{Y}$.

Removing the noise from the depth map is performed by locating the missing points and then replacing them using 2D cubic interpolation. Then, morphological filling is applied to the depth map. Those points whose difference with the filled image is larger than a threshold are assumed to be holes and are again replaced by cubic interpolation. This procedure helps to preserve the natural holes on the face, in particular near the eye's corners. Finally, median filtering with a 2.3mm $\times$ 2.3mm mask is used to remove the impulsive noise on the face's surface.

The next step is detection of the nose tip. To do this, the principal curvature and shape index (SI) are computed and the SI is scaled so that its maximum and minimum values are exactly +1 and -1, receptively. The face's convex regions are found by thresholding the SI to produce a binary image, using -1 $<$ SI $<$ $-\frac{5}{8}$ [3, 1, 5, 7]. The largest connected component is detected and its boundary is smoothed by dilating with a disk structuring element. Finally, the centroid is saved as the tip. The face region is eventually cropped after intersecting a sphere with radius 80mm, centered on the nose tip, with the face.

2.2. Alignment and nose cropping

The face region is aligned using the PCA based alignment algorithm of Mian *et al.* [6]. The Karhunen-Loève transform is performed on the face's point clouds. The points' mean is translated to the origin and their 3×3 covariance matrix calculated. The points are next mapped onto the principal axes after multiplying them by the covariance matrix's eigenvectors. They are then uniformly resampled with resolution 0.5 mm. The missing points caused by self-occlusion, which appear after applying the rotation, are replaced by 2D cubic interpolation in each iteration. The procedure is repeated until the 3×3 eigenvector matrix's Euclidean distance to the identity matrix is smaller than a threshold. In each iteration, the nose tip is re-detected. Therefore, after resampling, the SI is again calculated and the biggest convex region is located. The face

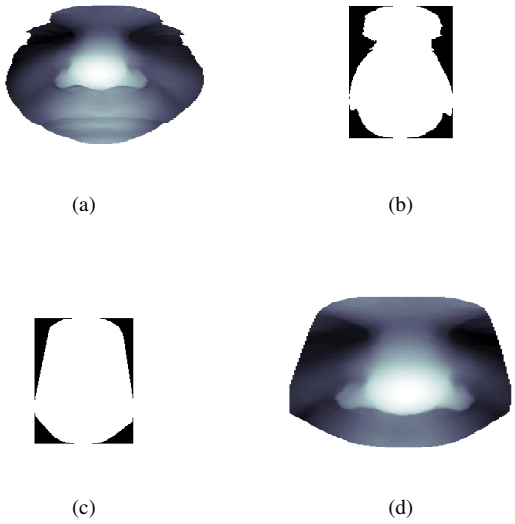

(a) (b) (c) (d)

Figure 1: (a) The cropped face region. (b) The binary map found by the cylinders intersection with the face surface. (c) The convex hull result. (d) The cropped nose region.

is again cropped and PCA is applied on the newly cropped image. This simple process helps to localise the tip more accurately. After the alignment procedure is completed a small constant angular rotation along the pitch direction is added to the face pose as this helps the landmarking algorithm to detect the nose root (radix).

The nose region is cropped by finding the intersections of three cylinders, each centered on the nose tip, with the face region. Two horizontal cylinders, with radii 40 mm and 70 mm, crop the lower and upper parts of the nose, respectively. Then, a vertical cylinder, of radius 50 mm, bounds the nose region on the left and right sides. Applying these conditions over the **X**, **Y** and **Z** maps results in a binary image [Fig. 1(b)], which is further trimmed by morphological filling and convex hull calculation [Fig. 1(c)]. The final binary image is used to find the cropped nose point clouds, see Fig. 1(d). This approach to nose region cropping results in fewer redundant regions than the approach of [5] and is much faster than that of [4] which uses level set based contours.

3. Nasal region landmarking and curves finding

Sixteen landmarks are detected on the nose region, as shown in Fig. 2. A cascade algorithm is used to directly find the nose tip (**L9**), root (**L1**), and the left (**L5**) and right (**L13**) extremities. First, **L9** is detected and then used to detect **L1**, **L5** and **L13**. To avoid selecting incorrect points resulting from residual noise or the nostrils as landmarks an

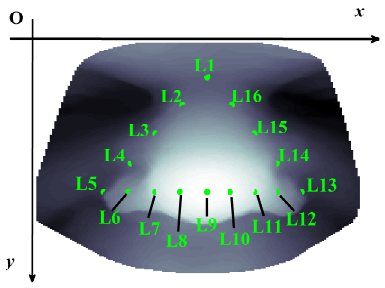

Figure 2: Landmarks' locations and names.

outlier removal procedure is employed and this procedure is explained in Section 3.4. The remainder of the landmarks are found by sub-dividing lines connecting the landmarks already found. In the following subsections the landmarking approach is explained in detail.

3.1. Nose tip L9 detection

Although the nose tip has already been approximately localised, it is more accurately fixed in this step. The SI is again thresholded to extract the largest convex regions from the cropped nose region. Then, the nose region's depth map, $\mathbf{Z_n}$, is inverted and the largest connected region is located [5]. The resulting binary image is multiplied by the convex region to refine it and remove noisy regions. The result is dilated with a disk structuring element and multiplied by $\mathbf{Z_n}$. After median filtering the result, the maximum point is considered as the nose tip. The reason for not directly selecting the maximum point of $\mathbf{Z_n}$ as the tip is its vulnerability to residual spike noise.

3.2. L1 detection

A set of planes perpendicular to the xy plane and containing **L9** are then found, as shown in Fig. 3. The angle between the i-th plane and the y-axis is denoted as α_i with a normal vector given by $[\cos\alpha_i, \sin\alpha_i, 0]$. Intersecting the nose surface and the planes results in a set of curves. The global minimum of each curve is found and the landmark **L1** is located at the maximum of the minima. This procedure is depicted in Fig. 3, in which α is the maximum value of $[\alpha_1, \alpha_2, \ldots, \alpha_M]$.

3.3. Detection of L5, L13 and the remaining landmarks

A set of planes, which include **L9**, are perpendicular to the xy plane and have the angular deviation β_i with the x-axis are intersected with the nose surface (Fig. 4). The normal of each planes is given by $[\sin\beta_i, \cos\beta_i, 0]$ and the intersection of the planes and the nose surface results in a

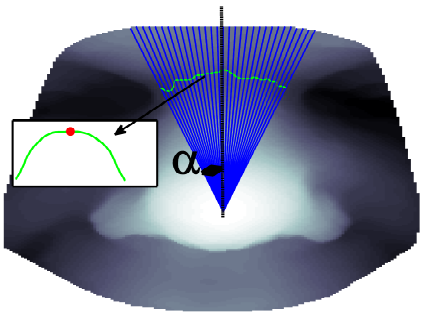

Figure 3: **L1** detection procedure: the blue lines are the planes intersection. The green curve is each intersection's minimum. The red dot is the minima peak, which gives the location of **L1** ($\alpha = 15°$).

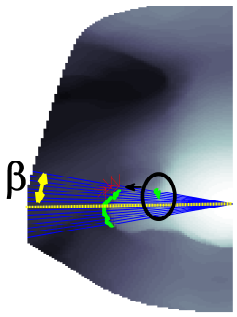

Figure 4: **L5** (and similarly **L13**) detection procedure: The blue lines: intersection of the orthogonal planes; The green points: candidate points for **L5**; The red points: the outlier removal result. $\beta = 15°$ is the maximum of $[\beta_1, \beta_2, \ldots, \beta_N]$

set of curves ($i = 1, \ldots, N$). **L5** and **L13** are located at the peak position of the curves' gradient. To do this, each curve is differentiated and the location of the peak values is stored. This results in a set of points on the sides of nasal alar from which the point with the minimum vertical distance from the nose tip (**L9**) are chosen as **L5** and **L13**.

After the four key landmarks were detected, they are projected on the *xy* plane. The lines connecting the projection of **L1** to **L5**, **L5** to **L9**, **L9** to **L13** and **L13** to **L1** are divided into four equal segments and the *x* and *y* positions of the resulting points are found. The corresponding points on the nose surface give the remaining landmark locations.

3.4. Removal of outlying landmark candidates

As the candidate positions for the landmarks **L5** and **L13** are the positions of maximum gradient on the nose surface, they are sensitive to noise and the position of the nostrils. In order to remove incorrect candidate positions an outlier removal algorithm is proposed. With reference to Fig. 4, the gradient maxima of the intersection of the planes with the nose surface are marked as green points. However, some outliers are detected as candidates for **L5**, in this case due to the impulsive depth change around the nose tip (located within the black circle in Fig. 4). To remove the outliers the distances from the candidate points to the nose tip are clustered using K-means with $K = 2$. The smallest cluster will contain the outliers and these points are then replaced by peaks in the surface gradient that are closer to the centroid of the larger cluster. The replacement candidates are plotted in red in Fig. 4.

A similar gradient-based approach for detecting the side nasal landmarks was proposed in [10], where the locations of the peaks of the gradient on the intersection of a horizontal plane passing through the tip and the nose surface were selected as **L5** and **L13**. However, by using a set of candidates instead of just a pair and the outlier removal, the approach proposed above is more robust.

3.5. Creating the nasal curves

After translating the origin of the 3D data to the nose tip, the landmarks are used to define a set of nasal curves that form the feature space for each nose. Considering any two pairs of landmarks, the intersection of a plane passing through the landmarks and perpendicular to the *xy* plane with the nose surface can be found. The normal vector of the plane is given by $\frac{(\mathbf{L_i}-\mathbf{L_k})\times\hat{a}_z}{|(\mathbf{L_i}-\mathbf{L_k})\times\hat{a}_z|}$, where $\mathbf{L_i}$ and $\mathbf{L_k}$ are the two landmarks and $\hat{a}_z$ is the unique vector of the *xy* plane. The 75 nasal curves depicted in Fig. 5 are found by connecting the following landmark pairs:

1. **L1** to **L2**-**L8** and **L10**-**L16**.
2. **L2** to **L6**-**L8** and **L10**-**L16**.
3. **L3** to **L16**, **L10** -**L15** and **L6**-**L8**.
4. **L4** to **L14**-**L16**, **L10**-**L13** and **L6**-**L8**.
5. **L5** to **L13**, and **L6**-**L7**.
6. **L9** to **L1**-**L5** and **L13**-**L16**.
7. **L14** to **L5**-**L8**, **L10**-**L12**.
8. **L15** to **L5**-**L8**, **L10**-**L12**.
9. **L16** to **L5**-**L8**, **L10**-**L12**.

Each curve is then resized to a fixed length and their maximum depth is translated to zero. The points from the complete set of 75 curves form the feature vector used for recognition.

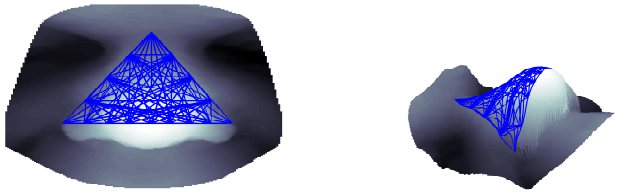

(a) (b)

Figure 5: The landmarks' connecting curves: (a) frontal view and (b) side view.

4. Expression robust feature selection

The set of nasal curves shown in Fig. 5 provide a fairly comprehensive coverage of the nasal surface. However, simply concatenating the curves produces a high dimensional feature vector that will typically suffer from the curse of dimensionality and so not produce the best classification performance. In addition, some of the curves are intrinsically more sensitive to the deformations caused by expression while others may be affected by the wearing of glasses, one of the most common occlusions found in biometrics sessions. Therefore, it is desirable to select a subset of curves that produce the best recognition performance over a range of expression variations and occlusions from glasses. By considering each curve as a set of features that are either included or excluded from the feature vector, the location of the nasal curves that contribute to a robust recognition performance can be investigated. To do this, the well-known Forward Sequential Feature Selection (FSFS) algorithm in employed. Using FSFS, the single curve that produces the best recognition performance is found and then different curves are iteratively added to form the set of the best n features. The cost function used to evaluate the recognition performance is

$$E = R_1. \tag{1}$$

where R_1 is the rank-one recognition rate. The ranks are obtained using the leave-one-out approach and nearest neighbor city-block (CB) distance calculation.

5. Experimental results

The quantitative evaluation of the NCM algorithm is provided in this section. The Bosphorus and FRGC v2.0 datasets are utilized for feature selection and matching, respectively. Two matching scenarios are used and the sensitivity to the number of training samples is analyzed.

Two 3D face datasets are used to evaluate the performance of the NCM algorithm. The first is FRGC v2.0 [8] which is one of the largest face datasets in terms of the number of subjects and has been extensively used for face recognition. The dataset includes 557 unique subjects, with slight pose and different expression variations. The data was captured using a Minolta Vivid 900/910 series sensor at three different time periods, Spring 2003, Fall 2003 and Spring 2004.

The second dataset is the Bosphorus dataset [9]. It consists of 4666 samples from 105 unique subjects, and includes many captures with occlusions and rotations in the pitch and yaw directions. The captures used a 3D structured-light based digitizer and, compared to FRGC, the faces in the Bosphorus dataset are less noisy and have more intense expression variations. Each subject has a set of frontal viewed samples having various expressions: neutral, happy, surprise, fear, sadness, anger and disgust. These samples are used below to select the most expression invariant curves.

5.1. Feature selection results

Feature selection is performed using FSFS and evaluated using the Bosphorus dataset. In all experiments, the facial curves were resampled to a fixed size of 50 points and concatenated to create the feature vector. Using a fixed number of points was found to produce a higher recognition performance than varying the number of points per curve according to the curves' length and the performance was also relatively insensitive to the number of points per curve.

Figure 6 plots the rank 1 recognition rate against the number of nasal curves in the feature set and also illustrates the curves selected for a number of points on the plot. For example, the first curve selected is that connecting **L1** to **L9** (**L1L9**) and then the combination of **L1L9** and **L4L13** produce the highest rank 1 performance.

Overall, the highest rank 1 recognition rate occurs when 28 curves are selected. The distribution of these curves, shown in Fig. 6, is relatively even over the nasal surface but is slightly denser on the nasal cartilage, which is less flexible due to its bony structure, and on the alar. After this, the rank 1 recognition rate decreases as more features are added which conforms with expectations. As these curves produce the best recognition performance for a dataset with a wide range of expressions, they should be relatively insensitive to variations in expression. These 28 robust curves, ordered by the FSFS result, are: **L9L1**, **L4L13**, **L5L13**, **L1L4**, **L15L5**, **L2L13**, **L1L14**, **L2L12**, **L3L6**, **L1L7**, **L9L5**, **L1L2**, **L16L8**, **L9L13**, **L3L16**, **L1L16**, **L16L5**, **L1L10**, **L16L6**, **L15L7**, **L16L12**, **L15L8**, **L14L12**, **L14L5**, **L1L5**, **L9L2**, **L15L11** and **L3L12**.

For comparison, a genetic algorithm (GA) is also used to select the best performing feature sets. First, a binary vector $\mathbf{W} = [w_1, w_2, \ldots, w_{75}]^T$ is created in which, for each of the 75 nasal curves,

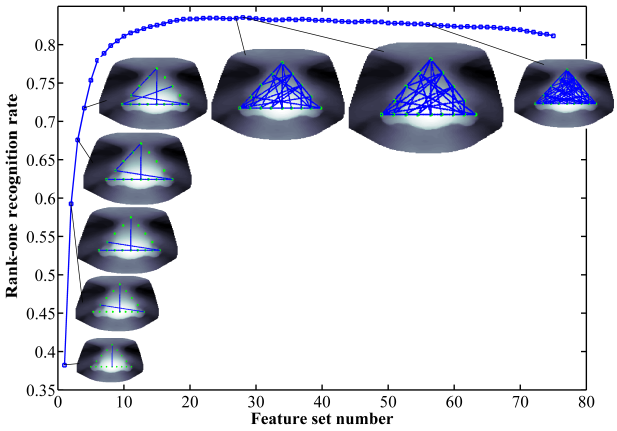

Figure 6: Rank 1 recognition rate against the number of nasal curves selected by the FSFS algorithm. The sets of curves for various numbers of feature sets are also shown, with the largest image (second from right) showing the 28 curves that produced the highest recognition rate.

$$w_i = \begin{cases} 1 & \text{if the } i\text{-th curve is selected} \\ 0 & \text{if the } i\text{-th curve is not selected} \end{cases} \quad (2)$$

and then a GA is used to maximize $\mathbf{W}$ using (1) as a measure of fitness.

Compared to FSFS, which is a deterministic algorithm, GA stochastically maximizes the rank 1 recognition rate. Although GA have the capability to examine various combinations of the features, its convergence is not guaranteed in a limited number of iterations. Cumulative Match Characteristic (CMC) recognition results for the best performing sets of curves selected be GA and FSFS are plotted in Fig. 7. The FSFS curves outperform those selected by GA in terms of recognition, computational speed and convergence. In addition, while the best performing FSFS set had only 28 curves, the GA set contained 33 curves.

5.2. Classification performance

The recognition performance of the NCM algorithm is evaluated using FRGC v2.0 dataset. In the experiments, the feature vectors are formed by concatenating the 28 expression robust curves found by FSFS on the Bosphorus dataset in the previous section, see Fig. 6. As before, all curves are resampled to 50 points and each curve is normalized by translating its maximum to zero.

Two scenarios are used to evaluate the NCM algorithm. The first one is the all-vs.-all scenario, in which all of the folders in the FRGC v2.0 dataset are merged. From the merged folders 505 subjects with at least two samples are

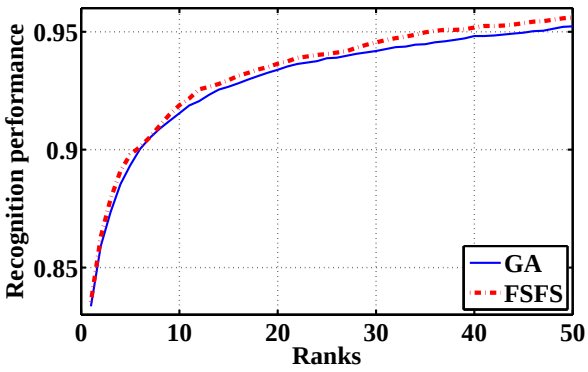

Figure 7: Cumulative match characteristic (CMC) curve for the best feature sets found by FSFS and GA feature selection results.

selected giving a total of 4879 samples. The number of training samples per class is varied from 1 to 12 and the rank 1 classification performance of a variety of classification methods found. The classification methods used are PCA, linear discriminant analysis (LDA), Kernel-Fisher's analysis (KFA), direct CB distance calculation, multi-class support vector machine (Multi-SVM) and bootstrap aggregating decision trees (TreeBagger). The PCA, LDA and KFA algorithms were implemented using the PhD toolbox (Pretty helpful Development functions for face recognition), while the Matlab's Statistics Toolbox is used for the SVM and TreeBagger classification. For the subspace classification methods, the final matching is performed using the nearest neighbor CB distance calculation.

Figure 8 shows the rank 1 recognition results for the all-vs.-all scenario. Matching using the direct calculation of the CB distance produces the worst recognition performance for ≥ 6 training samples. LDA and PCA project the feature space to a 277-dimensional subspace. These methods require a sufficient number of training samples per class to be trained appropriately [2] and for low numbers of training samples PCA fails to find the direction with the highest variance properly. This problem is more severe for LDA and is reflected in the low recognition rate for ≤ 5 training samples. However, as the number of training samples increases, the classification performance of these subspace projection techniques improves, in particular for LDA whose peak recognition rate reaches 97.78% for 12 training samples. To implement the multi-SVM classifier [13] the one-vs.-all scenario is used to generalize SVM to a multi-class classifier. Again for low number of iterations the recognition performance is low but dramatically increases with the number of training samples, up to 99.32% for 12 training samples. The TreeBagger classifier has the same trend, rising form a low rank 1 recognition rate for a sin-

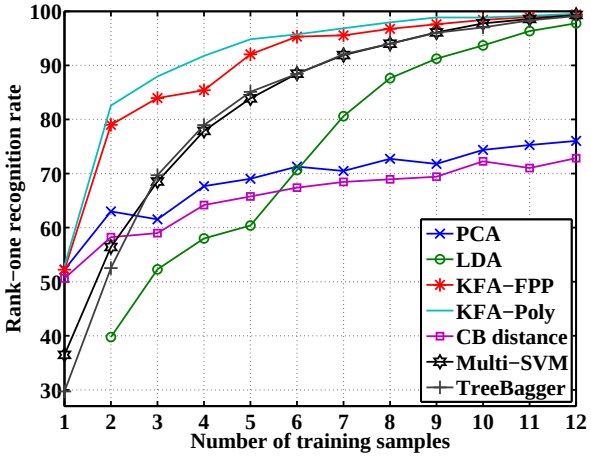

Figure 8: The rank-one recognition results using different numbers of training samples and classification methods.

gle training sample to 99.13% for 12 training samples. An ensemble of 119 trees are aggregated for the tree classifier. The issue of low training samples per class can be addressed by using kernels for Fisher's analysis [11]. Two kernels are used, the fractional power polynomial (FPP) kernel [12] and the polynomial (Poly) kernel. Figure 8 shows that both kernels result in a significant improvement in the recognition performance, with rank 1 rates of 82.58% and 79.01% for the Poly and FPP kernels, respectively, increasing to 99.5% for both kernels using 12 training samples.

The second scenario is based on the FRGC Experiment 3 [8]. The 3D samples in the Spring2003 folder, consisting of 943 samples from 275 subjects, are used for training and the other two folders are used for validation (4007 samples). Here, the only difference with the original Experiment 3 is that color or texture are not used so the NCM recognition algorithm only uses the 3D information. Two different experiments are performed: one using the neutral faces Fall2003 and Spring2004 folders as the probes and the other using the non-neutral samples in the probe folders. The receiver operating characteristic (ROC) curves and equal error rates (EER) for both neutral and non-neutral probes are given in Fig. 9 and Table 1, respectively. For the neutral probe images, KFA-Poly again produces the highest verification rate, with an EER of 0.05, compared to 0.08 for both PCA and direct nearest neighbor classification with the CB distance. LDA results in the poorest verification, again due to its sensitivity to few number of training samples.

When the non-neutral samples are used, the EER rate increases for all classification techniques. KFA-Poly still has the lowest EER at 0.18. Just above is the CB distance nearest neighbor classifier at 0.19 which performs better than PCA and LDA in this case. One reason for this could be

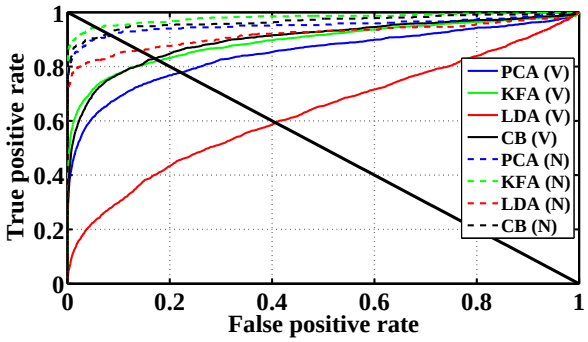

Figure 9: ROC curve for the neutral (dashed line - N) and non-neutral (solid line - V) samples.

Algorithm	Matching	Expression	
		Neutral	Varying
NCM	PCA	0.08	0.23
	KFA-Poly	**0.05**	**0.18**
	LDA	0.14	0.48
	CB	0.08	0.19
Chang *et al*. [1]	ICP	0.12	0.23

Table 1: EER found using Fig. 9.

that the CB distance has better discriminatory power when the feature space is sparse as it uses the L1-norm [14]. For comparison, the results of the nasal region facial verification result reported by Chang *et al*. [1] are provided. This work used the ICP algorithm for matching and the same dataset for verification. Its EER was reported as 0.12 and 0.23 for neutral and varying probes [1], which are 0.07 and 0.05 higher than the NCM EER using the KFA-Poly classification.

The final evaluation in Table 2 compares the rank 1 recognition rates achieved by the NCM algorithm with other nose region recognition results reported in the literature for neutral and varying expression probes. The comparison techniques and the results reported in the table are described in [1], [3], and [4]. When the size of the dataset is taken in to account, the NCM algorithm outperforms the other 3D nose recognition algorithms.

6. Summary and discussion

A new 3D face recognition algorithm using the shape of the nose region is proposed. The motivation for using the nose region is its relative invariance to variations in expressions. At the heart of the methods is a robust landmarking algorithm which is used to define 16 landmarks on the nose surface around the edge of the nose. By taking the landmarks in pairs, a set of 75 curves on the nose surface are generated and these form the feature set for matching. FSFS

Reference	Dataset	Expression	
		Neutral	Varying
Chang *et al*. [1]	FRGC v2.0	77.7% (PCA) 91% (ICP)	61.3% (PCA) 61.5% (ICP)
Drira *et al*. [4]	FRGC subset, 125 subjects	N/A	77% (Geodesic contours)
Dibeklioğlu *et al*. [3]	Bosphorus, 33 training samples/subject of 105 subjects	N/A	94.1% (ICP)
NCM	FRGC v2.0	90.10% (KFA-Poly) 87.13% (KFA-FPP)	80.01% (KFA-Poly) 70.74% (KFA-FPP)

Table 2: A comparison of NCM to some other nasal region recognition papers in the literature.

is applied to the feature set and 28 nasal curves that produce a robust performance over varying expressions are selected. These curves are used for verification and authentication scenarios, using a selection of classification algorithms. Results are obtained from two well-known 3D face dataset, FRGC v2.0 and Bosphorus dataset, show a high classification performance with low EER. Comparison with other reporting recognition results for the nasal region shows the high potential of our approach.

The current work can be extended in many aspects. Fusing the proposed feature space with the holistic facial features such as depth, Gabor wavelets or local binary patterns (LBP), has the potential for increasing the recognition performance. In addition, the NCM algorithm could also be used as a robust pattern rejector, to robustly reject many faces after computing their nasal region recognition ranks, hence reducing the complexity when very large datasets are used. Finally, the improvement in performance resulting from the fusion of NCM with baseline algorithm such as the Eigenfaces, Fisherfaces or ICP is an interesting extension of the work.

References

[1] K. Chang, W. Bowyer, and P. Flynn. Multiple nose region matching for 3D face recognition under varying facial expression. *IEEE Transactions on Pattern Analysis and Machine Intelligence*, 28(10):1695–1700, 2006.

[2] W. Deng, J. Hu, and J. Guo. Extended src: Undersampled face recognition via intraclass variant dictionary. *IEEE Transactions on Pattern Analysis and Machine Intelligence*, 34(9):1864–1870, 2012.

[3] H. Dibeklioğlu, B. Gökberk, and L. Akarun. Nasal region-based 3D face recognition under pose and expression variations. In *Proceedings of the Third International Conference on Advances in Biometrics*, pages 309–318, 2009.

[4] H. Drira, , B. Amor, M. Daoudi, and A. Srivastava. Nasal region contribution in 3D face biometrics using shape analysis framework. In *Proceedings of the Third International Conference on Advances in Biometrics*, pages 357–366, 2009.

[5] M. Emambakhsh and A. Evans. Self-dependent 3D face rotational alignment using the nose region. In *4th International Conference on Imaging for Crime Detection and Prevention 2011 (ICDP 2011)*, pages 1–6, 2011.

[6] A. Mian, M. Bennamoun, and R. Owens. An efficient multimodal 2D-3D hybrid approach to automatic face recognition. *IEEE Transactions on Pattern Analysis and Machine Intelligence*, 29(11):1927–1943, 2007.

[7] A. Moorhouse, A. Evans, G. Atkinson, J. Sun, and M. Smith. The nose on your face may not be so plain: Using the nose as a biometric. In *3rd International Conference on Crime Detection and Prevention (ICDP)*, pages 1–6, 2009.

[8] P. Phillips, P. Flynn, T. Scruggs, K. Bowyer, J. Chang, K. Hoffman, J. Marques, J. Min, and W. Worek. Overview of the face recognition grand challenge. In *IEEE Computer Society Conference on Computer Vision and Pattern Recognition (CVPR)*, pages 947– 954, 2005.

[9] A. Savran, N. Alyz, H. Dibeklioglu, O. eliktutan, B. Gkberk, B. Sankur, and L. Akarun. Bosphorus database for 3D face analysis. In *Biometrics and Identity Management*, volume 5372, pages 47–56. Springer Berlin / Heidelberg, 2008.

[10] M. Segundo, L. Silva, O. Bellon, and C. Queirolo. Automatic face segmentation and facial landmark detection in range images. *IEEE Transactions on Systems, Man, and Cybernetics*, 40(5):1319–1330, 2010.

[11] J. Tenenbaum, V. de Silva, and J. Langford. A global geometric framework for nonlinear dimensionality reduction. *Science*, 290(5500):2319–2323, 2000.

[12] V. Štruc and N. Pavešić. The complete gabor-fisher classifier for robust face recognition. *EURASIP Advances in Signal Processing*, 2010:26, 2010.

[13] J. Weston and C. Watkins. Multi-class support vector machines. In *Proceedings of ESANN99*, 1999.

[14] J. Wright, A. Yang, A. Ganesh, S. Sastry, and Y. Ma. Robust face recognition via sparse representation. *IEEE Transactions on Pattern Analysis and Machine Intelligence*, 31(2):210–227, 2009.

[15] S. Zafeiriou, M. Hansen, G. Atkinson, V. Argyriou, M. Petrou, M. Smith, and L. Smith. The photoface database. In *Computer Vision and Pattern Recognition Workshops (CVPRW), 2011 IEEE Computer Society Conference on*, pages 132–139, 2011.

[16] W. Zhao, R. Chellappa, P. Phillips, and A. Rosenfeld. Face recognition: A literature survey. *ACM Computing Surveys*, 35:399–458, 2003.